High-Order Harmonic Balance Vortex Lattice Method for Nonlinear Aeroelastic Limit Cycle Oscillations

S. Ayala*
Polytechnique Montréal, Montréal, Québec, H3T 0A3, Canada

M. Parenteau †
Bombardier Aerospace, Dorval, Québec, H4S 1Y9, Canada

E. Laurendeau ‡
Polytechnique Montréal, Montréal, Québec, H3T 0A3, Canada

This paper presents a full frequency-domain framework for nonlinear aeroelastic analysis that couples a high-order harmonic-balance (HB) structural solver with a recently developed HB Vortex-Lattice method (HB-VLM) for unsteady aerodynamics. Embedding this coupled solver within a numerical-continuation algorithm enables efficient tracing of self-sustained limit-cycle oscillations (LCOs) and their associated bifurcations without resorting to costly time-domain integration. The approach is demonstrated on canonical three-degree-of-freedom wing sections, where comparisons against time-marching solutions confirm that high-order HB captures rich harmonic content and bifurcation behavior. Our results highlight the method's accuracy and robustness even in strongly nonlinear regimes, along with paving the way for rapid medium-fidelity aeroelastic analysis of complex wings in early-stage aircraft design.

I. Nomenclature

a	=	dimensionless elastic axis location from mid-chord
b	=	semi-chord, m
c	=	dimensionless flap hinge location from mid-chord
c_{ref}	=	reference chord, m
ρ	=	air density, kg/m^3
C_L	=	lift coefficient
C_M	=	moment coefficient
h	=	plunge displacement, m
α	=	pitch angle, rad
β	=	flap deflection, rad
n_C	=	Fourier coefficients per DOF, $2n_H + 1$
n_D	=	number of degrees of freedom
n_H	=	number of harmonics
n_P	=	number of wing panels
n_S	=	number of AFT time samples
n_U	=	number of unknowns, $n_D \times n_C$
n_W	=	number of wake panels
S	=	reference area, m^2
t	=	time
U	=	freestream velocity, m/s
V	=	reduced velocity
Γ	=	vortex circulation

*M.Sc. Student, Department of Mechanical Engineering, samuel.ayala@polymtl.ca
†Engineering Professional, Department of Loads and Dynamics, matthieu.parenteau@aero.bombardier.com
‡Professor, Department of Mechanical Engineering, eric.laurendeau@polymtl.ca, AIAA Senior Member

$\boldsymbol{A}$ = wing panel influence matrix
$\boldsymbol{B}$ = wake influence matrix
$\boldsymbol{D}$ = discrete Fourier transform matrix
$\boldsymbol{M}$ = mass matrix
$\boldsymbol{C}$ = damping matrix
$\boldsymbol{K}$ = stiffness matrix
$\boldsymbol{R}$ = harmonic balance residual
$\boldsymbol{Z}$ = harmonic stiffness matrix
$\boldsymbol{\nabla}$ = harmonic differentiation operator
$\otimes$ = Kronecker product
$\boldsymbol{Y}$ = extended state vector
$\mathcal{G}$ = Phase condition equation
$\mathcal{P}$ = Parametrization equation
Δs = continuation step size
$\boldsymbol{z}$ = predictor vector
$\boldsymbol{e}$ = canonical basis vector
$\boldsymbol{H}$ = truncated Hill matrix
$\boldsymbol{J}$ = system Jacobian
$\boldsymbol{I}$ = identity matrix

II. Introduction

The introduction of lightweight, flexible wings [1] and control-surface architectures [2] has pushed modern aircraft into regimes where classical linear aeroelastic models start to lose fidelity. Localized effects such as hinge free-play, material hysteresis [3], and joint friction further add to the dynamical behavior. Under this combined structural and aerodynamic nonlinearity, wings can enter self-sustained limit-cycle oscillations (LCO) well below traditional flutter speeds, with potentially dangerous effects on structural integrity. Past research has shown that a surprisingly large number of harmonics is needed even for apparently simple cubic systems [4], and that time integration, time-domain orthogonal-collocation or shooting methods can become prohibitively expensive as system size grows [5]. At the same time, harmonic-balance methods (HBM) have proved to be both robust and numerically more efficient [6], though their use in aeroelasticity remains limited and typically confined to low-harmonic approximations or non-autonomous forced problems [7]. Likewise, most aeroelastic studies continue to employ reduced-order models in the frequency domain or state-space Wagner approximations in the time domain [8].

In this paper we bridge these gaps by developing a fully frequency-domain, 3D-ready, aeroelastic solver that couples high order harmonic balance for structures with nonlinearities with a recently developed harmonic-balance vortex-lattice method (HB-VLM) for the aerodynamics [9]. The solver is embedded in a continuation framework, enabling the capability to trace out complex LCO branches that undergo various types of bifurcations[10]: period-doubling cascades, fold points, and multi-valued response curves that cannot be solved for accurately with low order methods.

As initial results, we study a 2D wing sections with 3 degrees of freedom (pitch, plunge, and flap pitch), with either polynomial or free-play nonlinearities. We perform high-order HBM continuation and compare with time domain solutions in order to assess the accuracy of the proposed method. This novel approach opens the door to rapid, accurate nonlinear aeroelastic analysis early in the aircraft design cycle, and provides a foundation for future incorporation of even more complex flow and structural nonlinearities.

III. Methodology

A. Harmonic Balance Method

The dimensionless equations of motion of an n_D-degrees-of-freedom nonlinear aeroelastic system read:

$$\boldsymbol{M}\ddot{\boldsymbol{x}} + \boldsymbol{C}\dot{\boldsymbol{x}} + \boldsymbol{K}\boldsymbol{x} = \boldsymbol{f}(\boldsymbol{x}, \dot{\boldsymbol{x}}, t) \tag{1}$$

where $\boldsymbol{M}$, $\boldsymbol{C}$, $\boldsymbol{K}$ are the mass, damping, and stiffness matrices, and $\boldsymbol{f}$ represents the combined nonlinear structural and aerodynamic forces. The harmonic balance method determines the coefficients of a truncated Fourier series

approximating the periodic solution [11]:

$$\boldsymbol{x}(t) \simeq \frac{1}{2}\boldsymbol{a}_0 + \sum_{j=1}^{n_H} \left[\boldsymbol{a}_j \cos(j\omega t) + \boldsymbol{b}_j \sin(j\omega t)\right] \tag{2}$$

The frequency-domain coefficients are grouped as $\tilde{\boldsymbol{x}} = \left[\boldsymbol{a}_0, \boldsymbol{a}_1, \boldsymbol{b}_1, \ldots, \boldsymbol{a}_{n_H}, \boldsymbol{b}_{n_H}\right]^\top \in \mathbb{R}^{n_D n_C}$, with $n_C = 2n_H + 1$ coefficients per degree of freedom.

Substituting the Fourier expansion into (1) and applying Galerkin projection onto the Fourier basis yields the frequency-domain residual [12]:

$$\boldsymbol{R}(\tilde{\boldsymbol{x}}, \omega) = \boldsymbol{Z}(\omega)\tilde{\boldsymbol{x}} - \tilde{\boldsymbol{f}}(\tilde{\boldsymbol{x}}, \omega) = \boldsymbol{0} \tag{3}$$

where $\boldsymbol{Z}$ is the block-diagonal *harmonic stiffness* matrix:

$$\boldsymbol{Z}(\omega) = \omega^2 \boldsymbol{\nabla}^2 \otimes \boldsymbol{M} + \omega \boldsymbol{\nabla} \otimes \boldsymbol{C} + \boldsymbol{I}_{n_C} \otimes \boldsymbol{K} \tag{4}$$

in which $\otimes$ denotes the Kronecker product, $\boldsymbol{I}_{n_C}$ is the identity matrix of size n_C and $\boldsymbol{\nabla}$ is the global differential operator of $\boldsymbol{b}$ defined by:

$$\boldsymbol{\nabla} = \text{diagblock}\left(0, \boldsymbol{\nabla}_1, \ldots, \boldsymbol{\nabla}_j, \ldots, \boldsymbol{\nabla}_{n_H}\right) \quad \text{and} \quad \boldsymbol{\nabla}^2 = \boldsymbol{\nabla}\boldsymbol{\nabla} \tag{5}$$

with the elementary first-order derivative matrix $\boldsymbol{\nabla}_j$:

$$\nabla_j = j \begin{bmatrix} 0 & 1 \\ -1 & 0 \end{bmatrix} \text{ for } j \in [1..n_H] \tag{6}$$

The partial derivatives of the HB residual, needed for the extended system Jacobian, are defined as:

$$\begin{aligned} \frac{\partial \boldsymbol{R}}{\partial \tilde{\boldsymbol{x}}} &= \boldsymbol{Z}(\omega) - \frac{\partial \tilde{\boldsymbol{f}}}{\partial \tilde{\boldsymbol{x}}} \\ \frac{\partial \boldsymbol{R}}{\partial U} &= \left(\omega^2 \boldsymbol{\nabla}^2 \otimes \frac{\partial \boldsymbol{M}}{\partial U} + \omega \boldsymbol{\nabla} \otimes \frac{\partial \boldsymbol{C}}{\partial U} + \boldsymbol{I}_{n_C} \otimes \frac{\partial \boldsymbol{K}}{\partial U}\right) \tilde{\boldsymbol{x}} - \frac{\partial \tilde{\boldsymbol{f}}}{\partial U} \\ \frac{\partial \boldsymbol{R}}{\partial \omega} &= \left(2\omega \boldsymbol{\nabla}^2 \otimes \boldsymbol{M} + \boldsymbol{\nabla} \otimes \boldsymbol{C}\right) \tilde{\boldsymbol{x}} - \frac{\partial \tilde{\boldsymbol{f}}}{\partial \omega} \end{aligned} \tag{7}$$

where $\frac{\partial \tilde{\boldsymbol{f}}}{\partial \tilde{\boldsymbol{x}}}$, $\frac{\partial \tilde{\boldsymbol{f}}}{\partial U}$ and $\frac{\partial \tilde{\boldsymbol{f}}}{\partial \omega}$ are evaluated with central finite differences.

The frequency-domain forces $\tilde{\boldsymbol{f}}$ are computed using the Alternating Frequency-Time (AFT) scheme [13, 14]. The frequency-domain variables are first transformed to the time domain via inverse Fourier transform, where the nonlinear forces are evaluated at discrete time samples, then transformed back to the frequency domain. To prevent aliasing errors that occur from insufficient sampling, significant oversampling is employed.

B. Harmonic Balance Vortex Lattice Method

The Unsteay Vortex Lattice Method (UVLM) is a linearized potential flow method solving incompressible, inviscid and irrotational flows. Despite its simplicity, it finds many applications especially when coupled with viscous ans transonic flow databases. The Laplace equation is solved using a boundary element method that consists in the superposition of elementary flow singularities. The lifting surface is discretized in vortex rings and the Kutta condition is enforced through the modeling of the wake behind the wing as a surface of vortex rings with circulation values equal to previous time steps [15]. The UVLM equation consists to solving a linear system to obtain the lifting surface circulation coefficients $\Gamma(t)$:

$$\boldsymbol{A}\boldsymbol{\Gamma}(t) + \boldsymbol{B}\boldsymbol{\Gamma}_W(t) + (\boldsymbol{V} \cdot \boldsymbol{n}) = 0 \tag{8}$$

where $\boldsymbol{A} \in \mathbb{R}^{n_P \times n_P}$ is the aerodynamic influence coefficient matrix for bound vortex rings, $\boldsymbol{B} \in \mathbb{R}^{n_P \times n_W}$ is the wake influence coefficient matrix, $\boldsymbol{\Gamma} \in \mathbb{R}^{n_P}$ contains the unknown bound circulation strengths, $\boldsymbol{\Gamma}_W \in \mathbb{R}^{n_W}$ contains the known wake circulations from previous time steps, and $(\boldsymbol{V} \cdot \boldsymbol{n}) \in \mathbb{R}^{n_P}$ represents the normal velocity component at each panel collocation point.

The Harmonic Balance Vortex Lattice Method (HB-VLM) is a reformulation of the classical UVLM in the frequency domain without being linearized around a frozen geometry and isn't limited to small amplitude oscillations [16]. The circulation is formulated as a truncated Fourier series:

$$\boldsymbol{\Gamma}_j(t) = \sum_{k=0}^{N} \hat{\boldsymbol{\Gamma}}_{jk} \cdot e^{i\omega k t} \tag{9}$$

The substitution of eq.9 into the UVLM eq. 8 gives:

$$\boldsymbol{A} \sum_{k=0}^{N} \hat{\boldsymbol{\Gamma}}_k \cdot e^{i\omega k t} + \boldsymbol{B} \sum_{k=0}^{N} \hat{\boldsymbol{\Gamma}}_{TE,k} \cdot e^{i\omega k (t-(j+1)\Delta t} + \sum_{k=0}^{N} \hat{\boldsymbol{V}}_k \cdot e^{i\omega k t} \cdot \sum_{k=0}^{N} \hat{\boldsymbol{N}}_k \cdot e^{i\omega k t} = 0 \tag{10}$$

with $\boldsymbol{A}$ the wing-wing panel influence matrix, $\boldsymbol{B}$ the wing-wake influence matrix and $\boldsymbol{\Gamma}_{TE,k}$ denotes the circulation coefficients at the wing trailing edges.

Solving this equation directly involves the assembly of a large $(n_P \cdot n_C) \times (n_P \cdot n_C)$, which becomes rapidly untractable as the number of panels increases. Alternatively, the equation can be solved iteratively [9] by coupling the wake circulation through a Discrete Fourier Transform (DFT). This work goes a step further by assuming small deformations which allows the system to be reformulated as a matrix-product fixed point residual with a pre-factored influence matrix. Doing this reduces the memory usage by a factor of n_C^2.

$$\hat{\boldsymbol{\Gamma}}^{k+1} = \boldsymbol{A}^{-1} \boldsymbol{Q}^k \boldsymbol{D} \tag{11}$$

where $\boldsymbol{D}$ is the orthonormal real DFT transform matrix:

$$\boldsymbol{D} = \sqrt{\frac{2}{n}} \begin{bmatrix} \frac{1}{\sqrt{2}} & \cos(\omega t_1) & \sin(\omega t_1) & \cdots & \cos(\omega k t_1) & \sin(\omega k t_1) \\ \frac{1}{\sqrt{2}} & \cos(\omega t_2) & \sin(\omega t_2) & \cdots & \cos(\omega k t_2) & \sin(\omega k t_2) \\ \vdots & \vdots & \vdots & \ddots & \vdots & \vdots \\ \frac{1}{\sqrt{2}} & \cos(\omega t_n) & \sin(\omega t_n) & \cdots & \cos(\omega k t_n) & \sin(\omega k t_n) \end{bmatrix} \tag{12}$$

and $\boldsymbol{Q}$ contains the non-penetration condition and the wake influence expressed in time domain:

$$\boldsymbol{Q}_{ij} = -\left[\boldsymbol{V}_i \boldsymbol{N}_i + \boldsymbol{B} \boldsymbol{\Gamma}_W\right]_{t_j} \tag{13}$$

where $\boldsymbol{V}$ and $\boldsymbol{N}$ are the air flow velocity and unitary normal vector of each panel in global coordinates respectively. $\boldsymbol{\Gamma}_W$ is computed using the inverse transform of $\hat{\boldsymbol{\Gamma}}^k$. For better memory efficiency, the matrix vector product $\boldsymbol{B}\boldsymbol{\Gamma}_{\boldsymbol{W}}$ should be performed in a matrix-free fashion.

The HB-VLM fixed point eq. 11 is solved iteratively using $\hat{\boldsymbol{\Gamma}}^0 = 0$ as initial guess until convergence is reached. To improve on the linear rate of convergence of the simple fixed point iteration, the Anderson Acceleration (AA) [17] method is employed.

The aerodynamic forces are computed using the unsteady Joukowski method [18] which sums the steady and unsteady contributions to the aerodynamic load on each vortex ring:

$$\Delta \boldsymbol{F}_{ij} = \Delta \boldsymbol{F}_{steady} + \Delta \boldsymbol{F}_{unsteady} \tag{14}$$

The first term is given by the classical Kutta-Joukowski theorem [15], which relates the bound circulation to the lift force per unit span:

$$\Delta \boldsymbol{F}_{steady} = \rho \bar{\Gamma} (\boldsymbol{V} \times \boldsymbol{l}) \tag{15}$$

where $\bar{\Gamma}_{i,j} = \Gamma_{i,j} - \Gamma_{i-1,j}$ is the circulation difference between chord-wise consecutive panels, $\boldsymbol{V}$ is the local panel velocity and $\boldsymbol{l}$ is the bound vortex segment. The second term is:

$$\Delta \boldsymbol{F}_{unsteady} = \left(\rho \frac{\partial \Gamma}{\partial t} \Delta A\right) \boldsymbol{n} \tag{16}$$

where ΔA represents the panel area and $\boldsymbol{n}$ is the panel normal vector. The time derivatives of the circulation are computed using the Fourier coefficients as a compact matrix-matrix product with the DFT derivative matrix:

$$\frac{\partial \boldsymbol{\Gamma}}{\partial t} = \hat{\boldsymbol{\Gamma}} \left(\frac{\partial \boldsymbol{D}}{\partial t} \right)^{\top} \tag{17}$$

The total lift coefficient is obtained by projecting the panel forces onto the unit length lift axis $\boldsymbol{e}_L$ and normalizing by the dynamic pressure and reference area:

$$C_L = \frac{1}{\frac{1}{2}\rho V_\infty^2 S} \sum_i \sum_j \Delta \boldsymbol{F}_{ij} \cdot \boldsymbol{e}_L \tag{18}$$

Similarly, the moment coefficient about a reference point is computed as:

$$C_M = \frac{1}{\frac{1}{2}\rho V_\infty^2 S c_{ref}} \sum_i \sum_j (\boldsymbol{r}_{ij} - \boldsymbol{r}_{ref}) \times \Delta \boldsymbol{F}_{ij} \tag{19}$$

where $\boldsymbol{r}_{ij}$ denotes the force application point (typically the center of the leading vortex segment) and c_{ref} is the reference length that is usually the mean aerodynamic chord (MAC).

C. Continuation Framework

Coexisting stable solutions, with distinct limit cycle amplitudes, may arise at specific operating conditions, evidenced by amplitude jumps during freestream velocity sweeps [4]. To systematically trace these solution branches, the Harmonic Balance Method is combined with continuation techniques, enabling the prediction a series of steady state responses systematically. Continuation methods leverage prior solutions at adjacent parameter values to generate initial estimates for subsequent computations, progressively advancing through the parameter space. The technique employs a predictor-corrector algorithm, where a predicted solution is evaluated based on the previous solutions and a nonlinear root finding solver corrects the solution iteratively. Solving for the autonomous system requires the extension of the base unknowns with two extra variables: the fundamental response frequency ω and the freestream velocity U, the latter being the continuation parameter.

$$\boldsymbol{Y} = [\tilde{\boldsymbol{x}}, \omega, U]^T \tag{20}$$

The residual is extended by two additional equations that parametrize the two unknowns that have been added. To resolve the inherent phase ambiguity in autonomous systems arising from time-translation invariance, an orthogonal phase condition is introduced [12]. This condition is derived by enforcing orthogonality between the periodic solution and its time derivative, effectively minimizing phase drift relative to a reference trajectory.

$$\mathcal{G}_{i+1}^k = \sum_{j=1}^{n_H} j \left(\tilde{\boldsymbol{X}}_{i,2j} \tilde{\boldsymbol{X}}_{i+1,2j-1}^k - \tilde{\boldsymbol{X}}_{i,2k-1} \tilde{\boldsymbol{X}}_{i+1,2j}^k \right) = 0 \tag{21}$$

where $\tilde{\boldsymbol{X}}_{i,2j}$ means the $2j$-th column of the coefficient matrix of the i-th continuation step. For $d \in \{1, ..., n_H\}$ we define the column index intervals:

$$\mathcal{I}_d^{\text{odd}} = \left\{ (2d-1)n_D,\ (2d-1)n_D + 1,\ \ldots,\ 2dn_D - 1 \right\} \quad \text{and} \quad \mathcal{I}_d^{\text{even}} = \left\{ 2dn_D,\ 2dn_D + 1,\ \ldots,\ (2d+1)n_D - 1 \right\} \tag{22}$$

the partial derivative $\frac{\partial \mathcal{G}}{\partial \tilde{\boldsymbol{Y}}}$ can now be defined in parts:

$$\begin{aligned} \frac{\partial \mathcal{G}}{\partial \tilde{\boldsymbol{x}}}\bigg|_{\mathcal{I}_d^{\text{odd}}}^{j+1,k} &= d\, \tilde{\boldsymbol{X}}_{2d} & \frac{\partial \mathcal{G}}{\partial U} &= 0 \\ \frac{\partial \mathcal{G}}{\partial \tilde{\boldsymbol{x}}}\bigg|_{\mathcal{I}_d^{\text{even}}}^{j+1,k} &= -d\, \tilde{\boldsymbol{X}}_{2d-1} & \frac{\partial \mathcal{G}}{\partial \omega} &= 0 \end{aligned} \tag{23}$$

The parameterization equation constrains the continuation solver by enforcing a step-size-controlled predictor within a local hyper-sphere centered on the previous solution. This geometric condition ensures that the iterative correction

phase (e.g., via Newton-Raphson) remains well-conditioned, even near turning points or bifurcations where the system's Jacobian becomes singular [19].

$$\mathcal{P}\left(\boldsymbol{Y}_{i+1}^{k}\right) = \left\|\boldsymbol{Y}_{i+1}^{k} - \boldsymbol{Y}_{i}\right\|_{2}^{2} - \Delta s_{i}^{2} = 0 \tag{24}$$

where Δs is the step size. The derivative is defined as:

$$\frac{\partial \mathcal{P}}{\partial \boldsymbol{Y}} = 2\left(\boldsymbol{Y}_{i+1}^{k} - \boldsymbol{Y}_{i}\right) \tag{25}$$

forming our extended residual system from eqs. (3), (21) and (24):

$$\tilde{\boldsymbol{R}} = [\boldsymbol{R}, \mathcal{G}, \mathcal{P}]^{T} = 0 \tag{26}$$

and its Jacobian, calculated semi-analytically using the equations shown previously:

$$\frac{\partial \tilde{\boldsymbol{R}}}{\partial \tilde{\boldsymbol{x}}} = \begin{bmatrix} \frac{\partial \boldsymbol{R}}{\partial \hat{\boldsymbol{x}}} & \frac{\partial \boldsymbol{R}}{\partial U} & \frac{\partial \boldsymbol{R}}{\partial \omega} \\ \frac{\partial \mathcal{G}}{\partial \hat{\boldsymbol{x}}} & \frac{\partial \mathcal{G}}{\partial U} & \frac{\partial \mathcal{G}}{\partial \omega} \\ \frac{\partial \mathcal{P}}{\partial \hat{\boldsymbol{x}}} & \frac{\partial \mathcal{P}}{\partial U} & \frac{\partial \mathcal{P}}{\partial \omega} \end{bmatrix} \tag{27}$$

The tangent predictor estimates the direction of the solution branch by computing the local tangent vector to the equilibrium manifold at the current solution. This vector, derived from the null space of the augmented system's Jacobian matrix, provides a first-order approximation of the trajectory in the extended space.

$$\boldsymbol{Y}_{i+1}^{0} = \boldsymbol{Y}_{i} + \boldsymbol{z}_{i}\Delta s \tag{28}$$

where $\boldsymbol{z}$ is a unit length vector tangent to the solution branch, determined by solving the linear algebraic equation system using a least-squares solver for stability [19]:

$$\begin{bmatrix} \frac{\partial \tilde{\boldsymbol{R}}^{i}}{\partial \tilde{\boldsymbol{x}}^{i}} \\ \boldsymbol{c}^{\top} \end{bmatrix} \boldsymbol{z}_{i} = \begin{bmatrix} 0_{(n_E-1)\times 1} \\ 1 \end{bmatrix} \tag{29}$$

in which $\boldsymbol{c}$ is a unit vector defined as:

$$\boldsymbol{c} = \boldsymbol{e}_{i^*}, \quad \text{where} \quad i^* = \arg\max_{i} \left[\frac{|z_i^{j-1}|}{\max(|\tilde{\boldsymbol{x}}_i^{j-1}|, \epsilon)} \right] \tag{30}$$

with $\boldsymbol{e}_{i^*}$ the canonical basis vector (all zeros except 1 at index i^*) and $\epsilon = 10^{-4}$ ensures numerical stability. Additionally, the sign of the predictor may need to be flipped in case it points in the wrong direction [14].

The corrector step is defined as a Newton-Raphson step that is carried out by an advanced nonlinear root finding solver such as MINPACK's *hybr* routine that uses Powell's hybrid dogleg method with trust region [20].

Stability analysis of the response enables the characterization of the stability properties of the branch and identify various kinds of bifurcations [21]. In this work, the Floquet exponents are estimated in frequency domain using the truncated Hill matrix method. The eigenvalue problem is formulated as follows [22]:

$$(\boldsymbol{H} - \Lambda \boldsymbol{I}_{2n_U})\boldsymbol{Q} = \boldsymbol{0} \tag{31}$$

where the Hill matrix $\boldsymbol{H} \in \mathbb{R}^{2n_U \times 2n_U}$ is given by:

$$\boldsymbol{H} = \begin{bmatrix} \boldsymbol{0} & \boldsymbol{I}_{n_U} \\ -\boldsymbol{\Delta}_2^{-1}\boldsymbol{J} & -\boldsymbol{\Delta}_2^{-1}\boldsymbol{\Delta}_1 \end{bmatrix} \tag{32}$$

with the matrices:

$$\begin{aligned} \boldsymbol{\Delta}_2 &= \boldsymbol{I}_{n_C} \otimes \boldsymbol{M} \\ \boldsymbol{\Delta}_1 &= 2\omega\nabla \otimes \boldsymbol{M} + \boldsymbol{I}_{n_C} \otimes \boldsymbol{C} \end{aligned} \tag{33}$$

The eigenvalue problem yields $2n_U$ eigenvalues, but only $2n_D$ have physical meaning as approximations to the Floquet exponents. The remaining eigenvalues are artifacts of the harmonic truncation. The filtering approach implemented here selects eigenvalues based on the magnitude of their imaginary parts [23].

IV. Results

Numerical results are obtained for a three-degree-of-freedom (3-DOF) rigid wing model incorporating plunge, pitch, and control surface deflection as shown in Figure 1, with the parameters and equations listed in the Appendix. This model has been extensively studied in the literature, particularly in its linear configuration [24]. Linear stability analysis (omitted for brevity) identifies the flutter speed as $U_f = 23.96\ \mathrm{m\,s^{-1}}$ [25].

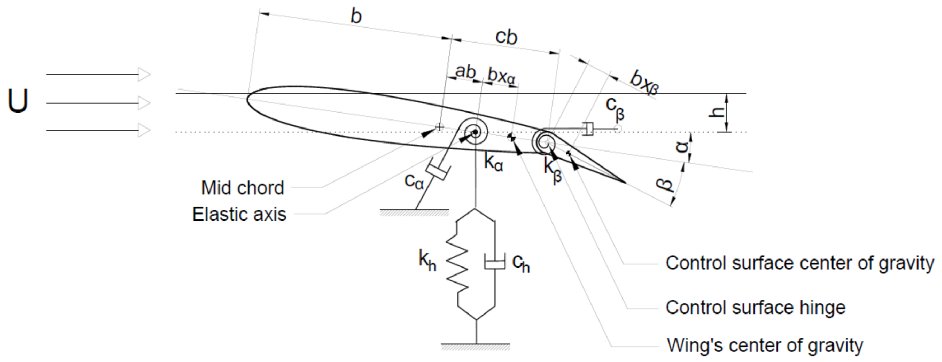

Fig. 1 Schematic of a 2D airfoil with control surface [25].

The aerodynamic forces from the 3D HB-VLM are mapped to the 2D wing through the following relation:

$$\boldsymbol{f_a} = \frac{V^2}{\pi} \begin{bmatrix} -C_L \\ 2\,C_{M_\alpha} \\ \frac{(1-c)^2}{2}\,C_{M_\beta} \end{bmatrix} \tag{34}$$

The nonlinearity is introduced through the control surface stiffness:

$$\boldsymbol{f_s} = \begin{bmatrix} 0 \\ 0 \\ -\left(\frac{\omega_\beta}{\omega_\alpha}\right)^2 r_\beta^2 \mathcal{M}(\beta) \end{bmatrix} \tag{35}$$

To establish baseline results, the continuation method is first applied to an HBM formulation of the Theodorsen model [24]. These results serve as a benchmark against which both time integration solutions and more advanced aerodynamic models can be compared. Subsequently, the analysis is extended to incorporate the HB-VLM results, which to our knowledge is a novel contribution to the literature.

Both the HB-Theodorsen and HB-VLM analyses employ 5 harmonics with 1536 sampling points per period for the AFT procedure. The HB-VLM implementation utilizes a refined mesh configuration consisting of 45 chordwise panels for the main wing surface and 15 chordwise panels for the flap, with both surfaces discretized using 2 spanwise panels. The wake extends over a length corresponding to 3 periods of periodic motion, ensuring adequate capture of unsteady aerodynamic effects.

Rather than employing the AFT procedure, the HB-VLM directly processes Fourier coefficients of the motion as input and generates corresponding Fourier coefficients of the aerodynamic forces as output. The iterative solution process within the HB-VLM occurs at each evaluation of the continuation residual.

A. Cubic Stiffness Nonlinearity

The cubic stiffness is modeled as a polynomial function of control surface deflection:

$$\mathcal{M}_p(\beta) = \beta_0 + \beta_1\beta + \beta_2\beta^2 + \beta_3\beta^3 \tag{36}$$

where $\beta_0 = \beta_1 = \beta_2 = 0$ and $\beta_3 = 1$ for this study.

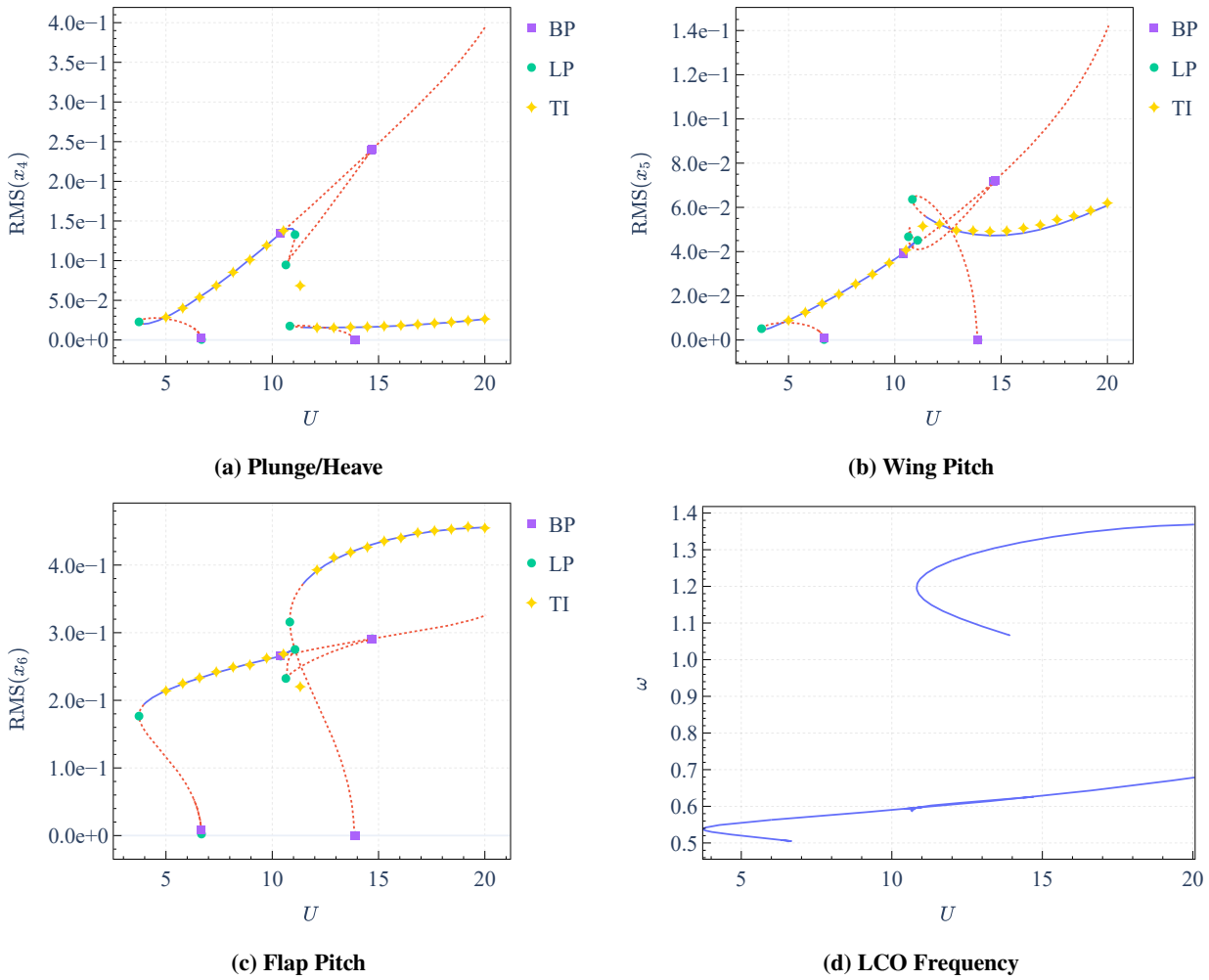

(a) Plunge/Heave **(b) Wing Pitch**

(c) Flap Pitch **(d) LCO Frequency**

Fig. 2 HB-Theodorsen results for the 3-DOF wing with flap cubic stiffness nonlinearity

While numerical continuation results for a pitching cubic stiffness nonlinearity for a 2-DOF wing have been presented very recently in the literature [26], to the authors' knowledge, no results for the numerical continuation of a 3-DOF wing with cubic stiffness nonlinearity have been published to date.

The results (Figure 2) are presented with stable regions indicated by solid lines and unstable regions by dashed lines. Branch Points (BP), Limit Points (LP), and Time Integration (TI) results are marked on the figure for reference. The response reveals rich nonlinear behavior with two distinct LCO branches emerging smoothly from the trivial solution branch. The upper branch exhibits additional complexity through a secondary branch. Time integration validates the stable branches; the isolated TI point near $U \approx 11.5$ corresponds to a chaotic transition zone between stable regimes.

Figure 3 demonstrates the usefulness of higher order harmonic-balance results for better correspondence with time integration results.

Figure 4 presents a comparison between the HB-Theodorsen and HB-VLM results. Both methods show good agreement for low-frequency oscillations ($\omega < 0.6$), with discrepancies emerging at higher frequencies where Theodorsen assumptions become less valid. Despite these differences, HB-VLM captures the overall branch topology, including multiple solution branches.

The premature termination of some HB-VLM branches results from the continuation algorithm's sensitivity to aerodynamic force accuracy. Relaxing the HB-VLM convergence tolerance from $\epsilon = 10^{-12}$ to 10^{-8} approximately triples the required continuation iterations, suggesting that a monolithic HB-VLM formulation [16] may offer improved robustness.

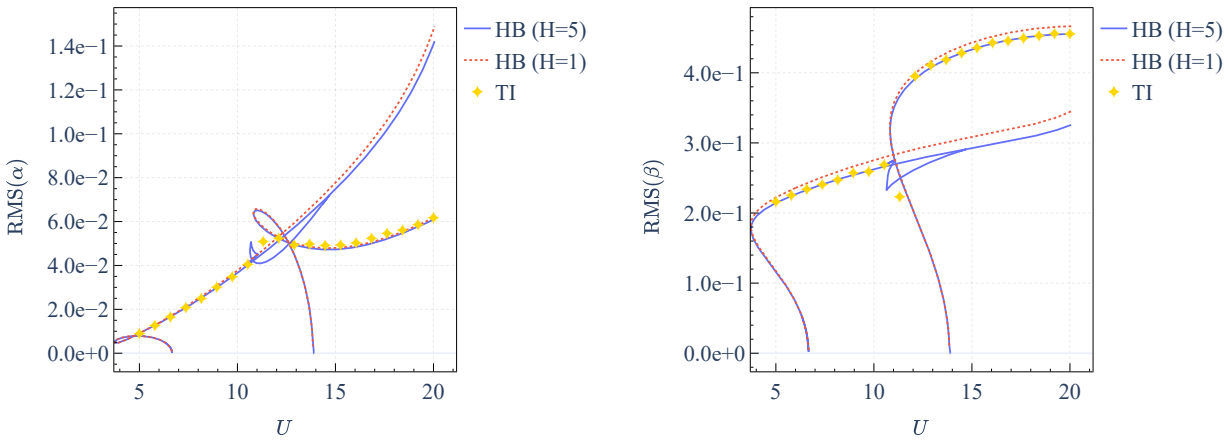

(a) Wing Pitch **(b) Flap Pitch**

Fig. 3 3-DOF Wing HB-Theodorsen with H=1 and H=5 solutions

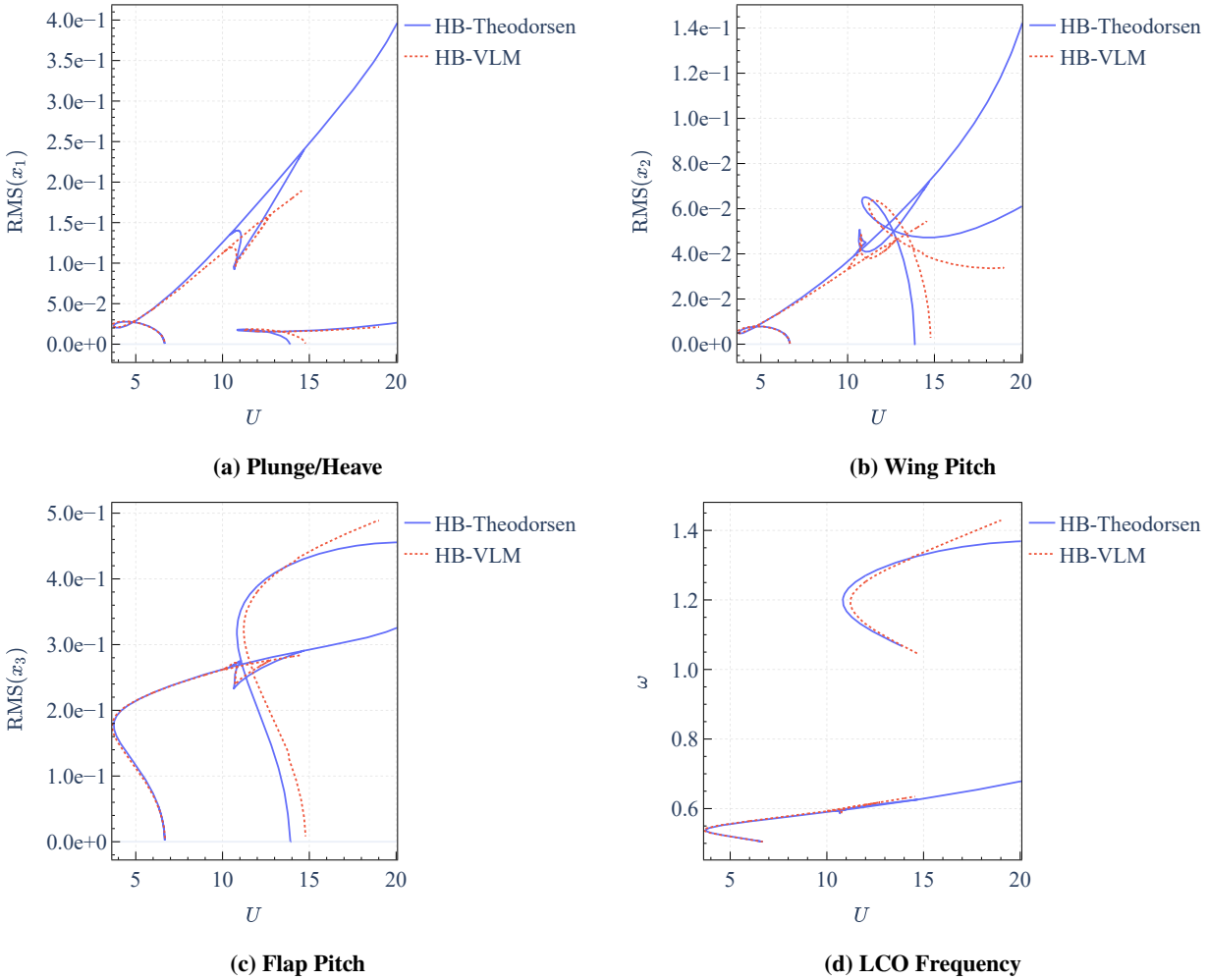

(a) Plunge/Heave **(b) Wing Pitch**

(c) Flap Pitch **(d) LCO Frequency**

Fig. 4 HB-Theodorsen and HB-VLM Comparison for the 3-DOF Wing with Flap Cubic Stiffness Nonlinearity

B. Freeplay Stiffness Nonlinearity

Following Conner's experimental study [4], the freeplay nonlinearity is defined as:

$$\mathcal{M}_f(\beta) = M_0 + \begin{cases} \beta - a_f & \text{if } \beta < a_f \\ M_f(\beta - a_f) & \text{if } a_f \le \beta \le a_f + \delta \\ \beta - a_f + \delta(M_f - 1) & \text{if } \beta > a_f + \delta \end{cases} \tag{37}$$

where $a_f = -2.12°$ is the freeplay offset, $\delta = 4.24°$ is the freeplay range, $M_f = 0$ is the freeplay stiffness, and $M_0 = 0$ is the preload.

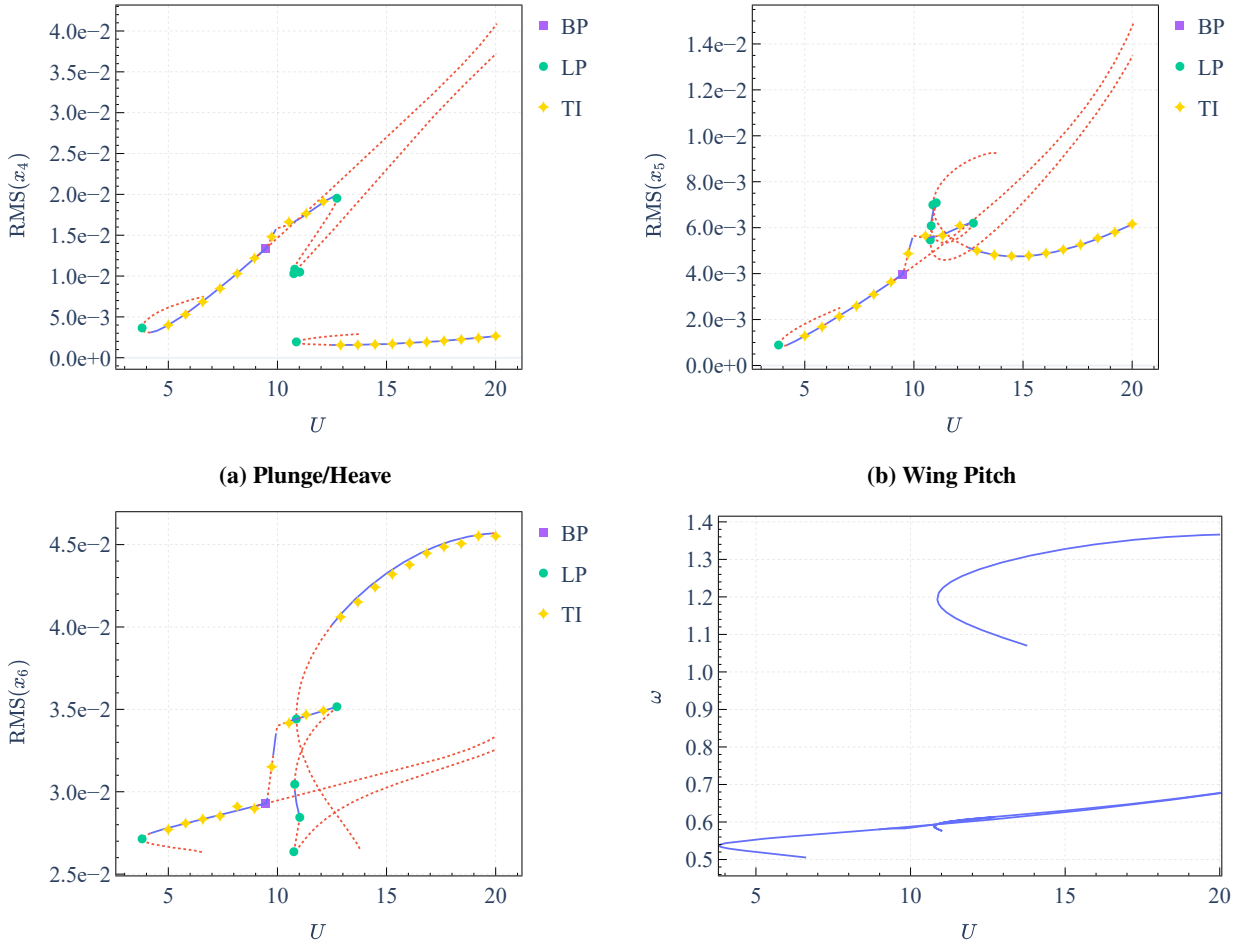

(a) Plunge/Heave

(b) Wing Pitch

(c) Flap Pitch

(d) LCO Frequency

Fig. 5 Continuation results for the 3-DOF wing with flap freeplay stiffness nonlinearity

HB-Theodorsen continuation results for a 3-DOF wing with flap freeplay stiffness have been previously reported in the literature [27]. However, these earlier analyses were incomplete, lacking identification of a critical secondary LCO branch and omitting essential bifurcation information and stability characteristics. To the authors' knowledge, the results presented here constitute the first comprehensive continuation analysis for a 3-DOF wing with flap freeplay stiffness nonlinearity, providing complete bifurcation mapping with full stability characterization of all solution branches.

The results, depicted in Figure 5, reveal two primary LCO branches that start abruptly by a jump from the trivial solution branch. The branches emerge at the same freestream velocities as in the cubic stiffness case as the onset of instability is governed by the same underlying linearized system [10]. The symmetry breaking pitchfork secondary bifurcation is observed again on the upper branch with the same detachment point but a different reattachment point.

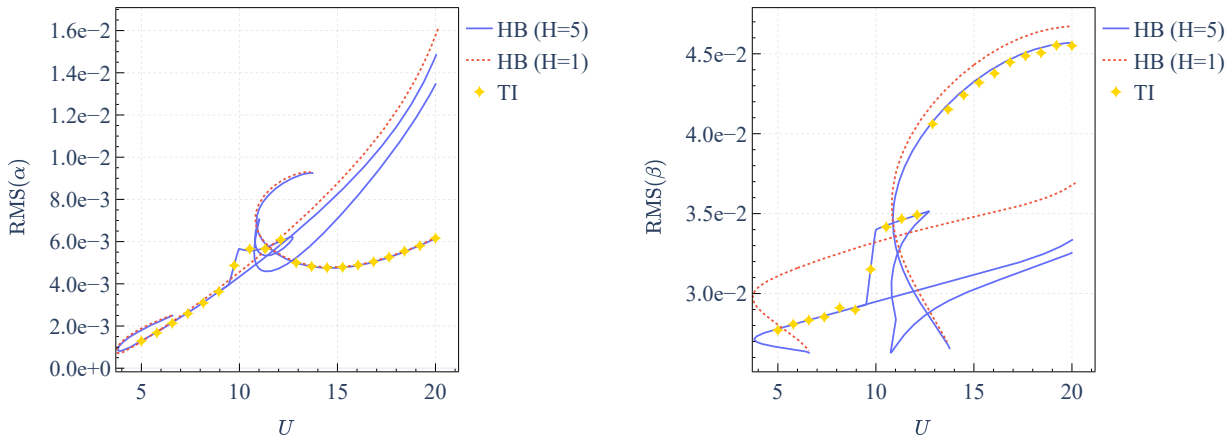

(a) Wing Pitch **(b) Flap Pitch**

Fig. 6 3-DOF Wing HB-Theodorsen with H=1 and H=5 solutions

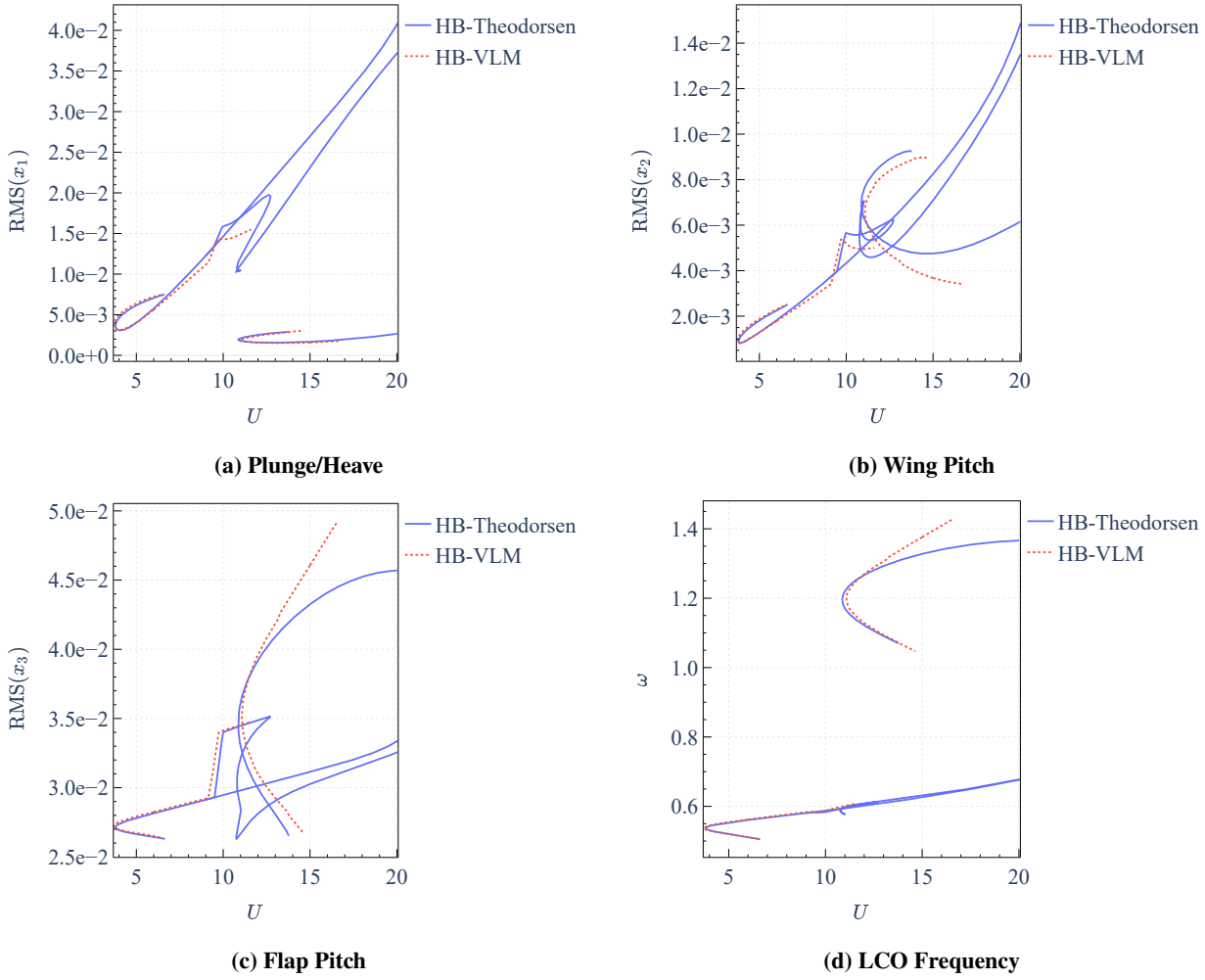

(a) Plunge/Heave **(b) Wing Pitch**

(c) Flap Pitch **(d) LCO Frequency**

Fig. 7 HB-Theodorsen and HB-VLM Comparison for the 3-DOF Wing with Flap Freeplay Stiffness Nonlinearity

Similarly to the cubic case, Figure 6 shows that the LCO harmonic content is rich and cannot be adequately represented by a single harmonic.

Figure 7 shows similar trends to those observed in the cubic stiffness case when comparing HB-Theodorsen and HB-VLM results. Correct agreement observed at low frequencies with discrepancies at higher frequencies.

V. Conclusion

In summary, this paper has demonstrated the application of a full frequency-domain approach to nonlinear aeroelasticity by coupling a high-order harmonic-balance structural solver with a harmonic-balance vortex-lattice aerodynamic model within a continuation framework. By applying the method to three-degree-of-freedom wing sections with both polynomial and free-play nonlinearities, we have shown that high-order harmonic balance accurately captures self-sustained LCO, including their rich harmonic content and bifurcation phenomena. The model is verified against time integration aeroelastic methods and confirms the method's accuracy. In particular, it captures in one case a critical secondary LCO branch not previously reported in the literature. Moreover, it removes the assumption of small angles and approximate wake function in the Theodorsen method. Looking ahead, this work paves the way for rapid, design-stage exploration of complex wing geometries, through the use of improved aerodynamic models like the NL-VLM method [28], and fully three-dimensional structural nonlinearities, thereby offering a powerful tool for next-generation aeroelastic aircraft design and analysis.

Appendix: 3-DOF Wing Equations

This appendix presents the complete set of parameters and the equations used in the aeroelastic analysis of the three-degree-of-freedom wing-flap system.

The values are taken from an experimental study by Conner et al. [4] and have been adapted to the chosen non-dimensional form of the equations of motion.

Some of the parameters listed in Table 1 are related through the following equations:

$$
\begin{aligned}
\mu &= \frac{m}{\pi\,\rho_\infty\,b^2}, & r_\alpha^2 &= \frac{I_\alpha}{m\,b^2}, & r_\beta^2 &= \frac{I_\beta}{m\,b^2},\\
k_h &= m\,\omega_h^2, & k_\alpha &= I_\alpha\,\omega_\alpha^2, & k_\beta &= I_\beta\,\omega_\beta^2,\\
\sigma &= \frac{\omega_h}{\omega_\alpha}, & V &= \frac{U}{b\,\omega_\alpha}, & C_h &= 2\,m\,\omega_h\,\zeta_h,\\
C_\alpha &= 2\,I_\alpha\,\omega_\alpha\,\zeta_\alpha, & C_\beta &= 2\,I_\beta\,\omega_\beta\,\zeta_\beta, & \tau &= \omega_\alpha\,t.
\end{aligned}
\tag{38}
$$

Given the dimensionless equation of motion:

$$
\boldsymbol{M_s}\ddot{\boldsymbol{q}} + \boldsymbol{C_s}\dot{\boldsymbol{q}} + \boldsymbol{K_s}\boldsymbol{q} = \boldsymbol{f}
\tag{39}
$$

where $\boldsymbol{q} = [h/b, \alpha, \beta]^T$ are the variables for the plunge, pitch and flap deflections respectively, and $\boldsymbol{f} = \boldsymbol{f_s} + \boldsymbol{f_a}$ is the total force vector including nonlinear structural and aerodynamic forces.

The dimensionless matrices are given by [25]:

$$
\begin{aligned}
\boldsymbol{M}_s &= \mu \begin{bmatrix} m_T/m & x_\alpha & x_\beta \\ x_\alpha & r_\alpha^2 & \left[(c-a)x_\beta + r_\beta^2\right] \\ x_\beta & \left[(c-a)x_\beta + r_\beta^2\right] & r_\beta^2 \end{bmatrix}\\
\boldsymbol{C}_s &= 2\mu \begin{bmatrix} \sigma\zeta_h & 0 & 0 \\ 0 & r_\alpha^2\zeta_\alpha & 0 \\ 0 & 0 & \frac{\omega_\beta}{\omega_\alpha} r_\beta^2 \zeta_\beta \end{bmatrix}\\
\boldsymbol{K}_s &= \mu \begin{bmatrix} \sigma^2 & 0 & 0 \\ 0 & r_\alpha^2 & 0 \\ 0 & 0 & \left(\frac{\omega_\beta}{\omega_\alpha}\right)^2 r_\beta^2 \end{bmatrix}
\end{aligned}
\tag{40}
$$

Table 1 System parameters for the three-degree-of-freedom aeroelastic model

Symbol	Description	Value	Unit
Geometric Parameters			
b	Semi-chord	0.127	m
a	Distance between mid-chord and elastic axis	-0.5	–
c	Distance between flap hinge and mid-chord	0.5	–
x_α	Distance between EA and center of gravity	0.4340	–
x_β	Distance between flap CG and flap hinge	0.02	–
Mass and Inertia Properties			
m	Mass of wing-aileron per unit span	1.5666	kg/m
m_t	Mass of wing-aileron and supports per unit span	3.39298	kg/m
I_α	Mass moment of inertia about wing EA per unit span	0.01347	kg·m
I_β	Mass moment of inertia about hinge per unit span	0.0003264	kg·m
μ	Mass ratio	31.8846	–
S_α	Static mass moment about wing EA per unit span	0.08587	kg
S_β	Static mass moment of flap about hinge per unit span	0.00395	kg
r_α	Radius of gyration around EA	0.7321	–
r_β	Radius of gyration around flap hinge	0.1140	–
Structural Properties			
k_h	Plunge stiffness coefficient	2818.8	kg/s^2
k_α	Pitch stiffness coefficient	37.34	kg·m^2/s^2
k_β	Flap stiffness coefficient	3.9	kg·m^2/s^2
ω_h	Uncoupled plunge natural frequency	42.5352	Hz
ω_α	Uncoupled pitch natural frequency	52.6506	Hz
ω_β	Uncoupled flap natural frequency	109.3093	Hz
σ	Frequency ratio	0.8080	–
ζ_h	Plunge damping ratio	0.0113	–
ζ_α	Pitch damping ratio	0.01626	–
ζ_β	Flap damping ratio	0.0115	–
Flow Properties			
ρ	Air density	1.225	kg/m^3
U	Freestream velocity	Variable	m/s
V	Reduced velocity	Variable	–

Note that in the case of a nonlinear degree of freedom, the stiffness matrix K_s must be modified accordingly to remove the linear stiffness term for that degree of freedom. In the case of a nonlinearity in the control surface, the structural force vector becomes:

$$\boldsymbol{f_s} = \begin{bmatrix} 0 \\ 0 \\ -\left(\frac{\omega_\beta}{\omega_\alpha}\right)^2 r_\beta^2 \mathcal{M}(\beta) \end{bmatrix} \tag{41}$$

where $\mathcal{M}(\beta)$ is a nonlinear moment function defined by the user.

The aerodynamic forces are obtained from either the HB-VLM or Theodorsen's model. For the latter the aerodynamic

forces are given by:

$$\boldsymbol{f_a} = \boldsymbol{M}_a\ddot{\boldsymbol{q}} + \boldsymbol{C}_a\dot{\boldsymbol{q}} + \boldsymbol{K}_a\boldsymbol{q} + \boldsymbol{L}_\delta\boldsymbol{b} \tag{42}$$

The generalized Theodorsen function is represented by Wagner's function $\Phi(t)$ [29] and computed using Jones' approximation [30].

$$\Phi(t) = 1 - \delta_1 e^{-\lambda_1 \frac{U}{b} t} - \delta_2 e^{-\lambda_2 \frac{U}{b} t} \tag{43}$$

with the coefficients $\delta_1 = 0.165$, $\delta_2 = 0.335$, $\lambda_1 = 0.0455$, $\lambda_2 = 0.3$. This yields two additional lag states $\boldsymbol{b} = [b_1, b_2]^T$ associated to the unsteady aerodynamics along with their differential equation definition.

$$\dot{\boldsymbol{b}} = \boldsymbol{Q}_a\ddot{\boldsymbol{q}} + \boldsymbol{Q}_v\dot{\boldsymbol{q}} + \boldsymbol{L}_\lambda\boldsymbol{b} \tag{44}$$

All the matrices are defined below:

$$\begin{aligned}
\boldsymbol{M}_a &= \begin{bmatrix} -1 & a & \frac{T_1}{\pi} \\ a & -\left(\frac{1}{8} + a^2\right) & -\frac{2T_{13}}{\pi} \\ \frac{T_1}{\pi} & -\frac{2T_{13}}{\pi} & \frac{T_3}{\pi^2} \end{bmatrix} \\
\boldsymbol{C}_a &= V \begin{bmatrix} -2 & -2(1-a) & \frac{T_4 - T_{11}}{\pi} \\ 1 + 2a & a(1-2a) & \frac{1}{\pi}\left(T_8 - T_1 + (c-a)T_4 + aT_{11}\right) \\ -\frac{T_{12}}{\pi} & \frac{1}{\pi}\left(2T_9 + T_1 + (T_{12} - T_4)\left(a - \frac{1}{2}\right)\right) & \frac{T_{11}}{2\pi^2}\left(T_4 - T_{12}\right) \end{bmatrix} \\
\boldsymbol{K}_a &= V^2 \begin{bmatrix} 0 & -2 & -\frac{2T_{10}}{\pi} \\ 0 & 1 + 2a & \frac{1}{\pi}\left(2aT_{10} - T_4\right) \\ 0 & -\frac{T_{12}}{\pi} & -\frac{1}{\pi^2}\left(T_5 - T_{10}\left(T_4 - T_{12}\right)\right) \end{bmatrix} \\
\boldsymbol{L}_\delta &= 2V \begin{bmatrix} \delta_1 & \delta_2 \\ -\left(\frac{1}{2} + a\right)\delta_1 & -\left(\frac{1}{2} + a\right)\delta_2 \\ \frac{T_{12}\delta_1}{2\pi} & \frac{T_{12}\delta_2}{2\pi} \end{bmatrix} \\
\boldsymbol{Q}_a &= \begin{bmatrix} 1 & \frac{1}{2} - a & \frac{T_{11}}{2\pi} \\ 1 & \frac{1}{2} - a & \frac{T_{11}}{2\pi} \end{bmatrix} \\
\boldsymbol{Q}_v &= V \begin{bmatrix} 0 & 1 & \frac{T_{10}}{\pi} \\ 0 & 1 & \frac{T_{10}}{\pi} \end{bmatrix} \\
\boldsymbol{L}_\lambda &= V \begin{bmatrix} -\lambda_1 & 0 \\ 0 & -\lambda_2 \end{bmatrix}
\end{aligned} \tag{45}$$

With the auxiliary terms given by Theodorsen [24]:

$$
\begin{aligned}
T_1 &= -\frac{1}{3}\sqrt{1-c^2}\left(2+c^2\right) + c\cos^{-1}(c) \\
T_2 &= c\left(1-c^2\right) - \sqrt{1-c^2}\left(1+c^2\right)\cos^{-1}(c) + c\left[\cos^{-1}(c)\right]^2 \\
T_3 &= -\left(\frac{1}{8}+c^2\right)\left[\cos^{-1}(c)\right]^2 + \frac{1}{4}c\sqrt{1-c^2}\cos^{-1}(c)\left(7+2c^2\right) - \frac{1}{8}\left(1-c^2\right)\left(5c^2+4\right) \\
T_4 &= -\cos^{-1}(c) + c\sqrt{1-c^2} \\
T_5 &= -\left(1-c^2\right) - \left[\cos^{-1}(c)\right]^2 + 2c\sqrt{1-c^2}\cos^{-1}(c) \\
T_6 &= T_2 \\
T_7 &= -\left(\frac{1}{8}+c^2\right)\cos^{-1}(c) + \frac{1}{8}c\sqrt{1-c^2}\left(7+2c^2\right) \\
T_8 &= -\frac{1}{3}\sqrt{1-c^2}\left(2c^2+1\right) + c\cos^{-1}(c) \\
T_9 &= \frac{1}{2}\left[\frac{1}{3}\left(1-c^2\right)^{\frac{3}{2}} + aT_4\right] \\
T_{10} &= \sqrt{1-c^2} + \cos^{-1}(c) \\
T_{11} &= \cos^{-1}(c)(1-2c) + \sqrt{1-c^2}(2-c) \\
T_{12} &= \sqrt{1-c^2}(2+c) - \cos^{-1}(c)(1+2c) \\
T_{13} &= \frac{1}{2}\left[-T_7 - (c-a)T_1\right] \\
T_{14} &= \frac{1}{16} + \frac{1}{2}ac
\end{aligned}
\tag{46}
$$

To integrate the coupled equations of motion with lag states, the system is reformulated as a first-order system:

$$
\dot{\boldsymbol{y}} = \boldsymbol{B}^{-1}\left[\boldsymbol{A}\boldsymbol{y} + \boldsymbol{f}(\boldsymbol{y})\right] \tag{47}
$$

with the state vector $\boldsymbol{y} = [\dot{\boldsymbol{q}}^T, \boldsymbol{q}^T, \boldsymbol{b}^T]^T$. The matrix $\boldsymbol{A}$ is defined as:

$$
\boldsymbol{A} = \begin{bmatrix} \boldsymbol{C}_a - \boldsymbol{C}_s & \boldsymbol{K}_a - \boldsymbol{K}_s & \boldsymbol{L}_\delta \\ \boldsymbol{I}_{3\times3} & \boldsymbol{0}_{3\times3} & \boldsymbol{0}_{3\times2} \\ \boldsymbol{Q}_v & \boldsymbol{0}_{2\times3} & \boldsymbol{L}_\lambda \end{bmatrix} \tag{48}
$$

the matrix $\boldsymbol{B}$ is defined as:

$$
\boldsymbol{B} = \begin{bmatrix} \boldsymbol{M}_s - \boldsymbol{M}_a & \boldsymbol{0}_{3\times3} & \boldsymbol{0}_{3\times2} \\ \boldsymbol{0}_{3\times3} & \boldsymbol{I}_{3\times3} & \boldsymbol{0}_{3\times2} \\ -\boldsymbol{Q}_a & \boldsymbol{0}_{2\times3} & \boldsymbol{I}_{2\times2} \end{bmatrix} \tag{49}
$$

and finally the extended force vector is defined as:

$$
\boldsymbol{f}(\boldsymbol{y}) = \begin{bmatrix} \boldsymbol{f_s} \\ 0_{3\times1} \end{bmatrix} \tag{50}
$$

Acknowledgments

This work benefited from the financial support from Bombardier Aerospace, Canada, and MITACS, Canada.

References

[1] Patil, M. J., and Hodges, D. H., "On the importance of aerodynamic and structural geometrical nonlinearities in aeroelastic behavior of high-aspect-ratio wings," *Journal of Fluids and Structures*, Vol. 19, No. 7, 2004, pp. 905–915. https://doi.org/10.1016/j.jfluidstructs.2004.04.012.

[2] Padmanabhan, M., Dowell, E., and Pasiliao, C., "Computational study of aeroelastic limit cycles due to localized structural nonlinearities," *Journal of Aircraft*, Vol. 55, No. 4, 2018, pp. 1531–1541. https://doi.org/10.2514/1.C034645.

[3] Gilioli, A., Manes, A., Ringertz, U., and Giglio, M., "Investigation about the structural nonlinearities of an aircraft pylon," *Journal of Aircraft*, Vol. 56, No. 1, 2019, pp. 273–283. https://doi.org/10.2514/1.C034882.

[4] Conner, M., Tang, D., Dowell, E., and Virgin, L., "NONLINEAR BEHAVIOR OF A TYPICAL AIRFOIL SECTION WITH CONTROL SURFACE FREEPLAY: A NUMERICAL AND EXPERIMENTAL STUDY," *Journal of Fluids and Structures*, Vol. 11, No. 1, 1997, pp. 89–109. https://doi.org/10.1006/jfls.1996.0068, URL https://linkinghub.elsevier.com/retrieve/pii/S0889974696900687.

[5] Lee, B. H. K., Price, S. J., and Wong, Y. S., "Nonlinear aeroelastic analysis of airfoils: bifurcation and chaos," *Progress in Aerospace Sciences*, Vol. 35, No. 3, 1999, pp. 205–334. https://doi.org/10.1016/S0376-0421(98)00015-3, URL https://www.sciencedirect.com/science/article/pii/S0376042198000153.

[6] Gudmundson, P., "On the accuracy of the harmonic balance method concerning vibrations of beams with nonlinear supports," *Ingenieur-Archiv*, Vol. 59, No. 5, 1989, pp. 333–344. https://doi.org/10.1007/BF00534063, URL https://doi.org/10.1007/BF00534063.

[7] Lanza, V., Bonnin, M., and Gilli, M., "On the Application of the Describing Function Technique to the Bifurcation Analysis of Nonlinear Systems," *IEEE Transactions on Circuits and Systems II: Express Briefs*, Vol. 54, No. 4, 2007, pp. 343–347. https://doi.org/10.1109/TCSII.2006.890406, URL https://ieeexplore.ieee.org/document/4155062.

[8] Murua, J., "Flexible Aircraft Dynamics with a Geometrically-Nonlinear Description of the Unsteady Aerodynamics," Ph.D. thesis, Jun. 2012.

[9] Parenteau, M., and Laurendeau, E., "A general modal frequency-domain vortex lattice method for aeroelastic analyses," *Journal of Fluids and Structures*, Vol. 99, 2020, p. 103146. https://doi.org/10.1016/j.jfluidstructs.2020.103146, URL https://linkinghub.elsevier.com/retrieve/pii/S0889974620306150.

[10] Dimitriadis, G., *Introduction to Nonlinear Aeroelasticity*, Wiley, 2017. Google-Books-ID: z8NlswEACAAJ.

[11] Urabe, M., "Galerkin's procedure for nonlinear periodic systems," *Archive for Rational Mechanics and Analysis*, Vol. 20, No. 2, 1965, pp. 120–152. https://doi.org/10.1007/BF00284614, URL https://doi.org/10.1007/BF00284614.

[12] Dimitriadis, G., "Continuation of Higher-Order Harmonic Balance Solutions for Nonlinear Aeroelastic Systems," *Journal of Aircraft*, Vol. 45, No. 2, 2008, pp. 523–537. https://doi.org/10.2514/1.30472, URL https://arc.aiaa.org/doi/10.2514/1.30472.

[13] Cameron, T. M., and Griffin, J. H., "An Alternating Frequency/Time Domain Method for Calculating the Steady-State Response of Nonlinear Dynamic Systems," *Journal of Applied Mechanics*, Vol. 56, No. 1, 1989, pp. 149–154. https://doi.org/10.1115/1.3176036.

[14] Krack, M., and Gross, J., *Harmonic Balance for Nonlinear Vibration Problems*, Mathematical Engineering, Springer International Publishing, Cham, 2019. https://doi.org/10.1007/978-3-030-14023-6, URL http://link.springer.com/10.1007/978-3-030-14023-6.

[15] Katz, J., and Plotkin, A., *Low-Speed Aerodynamics*, 2nd ed., Cambridge Aerospace Series, Cambridge University Press, Cambridge, 2001. https://doi.org/10.1017/CBO9780511810329, URL https://www.cambridge.org/core/books/lowspeed-aerodynamics/077FAF851C4582F1B7593809752C44AE.

[16] Parenteau, M., "A Non-Linear Frequency Domain Potential Flow Model for Compressible, Transonic and Viscous Aeroelastic Analyses," phd, Polytechnique Montréal, May 2021. URL https://publications.polymtl.ca/6629/.

[17] Walker, H. F., and Ni, P., "Anderson Acceleration for Fixed-Point Iterations," *SIAM Journal on Numerical Analysis*, Vol. 49, No. 4, 2011, pp. 1715–1735. https://doi.org/10.1137/10078356X, URL http://epubs.siam.org/doi/10.1137/10078356X.

[18] Simpson, R. J. S., Palacios, R., and Murua, J., "Induced-Drag Calculations in the Unsteady Vortex Lattice Method," *AIAA Journal*, Vol. 51, No. 7, 2013, pp. 1775–1779. https://doi.org/10.2514/1.J052136, URL https://arc.aiaa.org/doi/10.2514/1.J052136, publisher: American Institute of Aeronautics and Astronautics.

[19] Seydel, R., "Principles of Continuation," *Practical Bifurcation and Stability Analysis*, edited by R. Seydel, Springer, New York, NY, 2010, pp. 169–198. https://doi.org/10.1007/978-1-4419-1740-9_4, URL https://doi.org/10.1007/978-1-4419-1740-9_4.

[20] Moré, J. J., Garbow, B. S., and Hillstrom, K. E., "User Guide for MINPACK-1," Tech. Rep. ANL-80-74, Argonne National Laboratory, Argonne, Ill., 1980.

[21] Colaïtis, Y., and Batailly, A., "The harmonic balance method with arc-length continuation in blade-tip/casing contact problems," *Journal of Sound and Vibration*, 2021, p. 116070. https://doi.org/10.1016/j.jsv.2021.116070, URL https://hal.science/hal-03163560, publisher: Elsevier.

[22] Delbé, C., "Application d'une stratégie numérique de suivi de bifurcations à l'analyse d'interactions aube/carter dans les moteurs d'avions," Master's thesis, Polytechnique Montréal, Jul. 2023. URL https://publications.polymtl.ca/54150/.

[23] Zhou, J., Hagiwara, T., and Araki, M., "Spectral characteristics and eigenvalues computation of the harmonic state operators in continuous-time periodic systems," *Systems & Control Letters*, Vol. 53, No. 2, 2004, pp. 141–155. https://doi.org/10.1016/j.sysconle.2004.03.002, URL https://www.sciencedirect.com/science/article/pii/S0167691104000532.

[24] Theodorsen, T., "General Theory of Aerodynamic Instability and the Mechanism of Flutter," Tech. Rep. NACA-TR-496, Jan. 1949. URL https://ntrs.nasa.gov/citations/19930090935, nTRS Author Affiliations: National Advisory Committee for Aeronautics. Langley Aeronautical Lab. NTRS Document ID: 19930090935 NTRS Research Center: Legacy CDMS (CDMS).

[25] Darabseh, T. T., "Nonlinear State Dependent Riccati Equation Controller for 3-DOF Airfoil with Cubic Structural Nonlinearity," *International Review of Aerospace Engineering (IREASE)*, Vol. 15, No. 2, 2022, pp. 97–111. https://doi.org/10.15866/irease.v15i2.21426, URL https://www.praiseworthyprize.org/jsm/index.php?journal=irease&page=article&op=view&path[]=26230, publisher: Praise Worthy Prize.

[26] McGurk, M., and Yuan, J., "Prediction and validation of aeroelastic limit cycle oscillations using harmonic balance methods and Koopman operator," *Nonlinear Dynamics*, 2025. https://doi.org/10.1007/s11071-025-11065-8, URL https://doi.org/10.1007/s11071-025-11065-8.

[27] Liu, L., and Dowell, E. H., "High Dimensional Harmonic Balance Analysis for Dynamic Piecewise Aeroelastic Systems," American Society of Mechanical Engineers Digital Collection, 2009, pp. 659–669. https://doi.org/10.1115/IMECE2008-66681, URL https://dx.doi.org/10.1115/IMECE2008-66681.

[28] Liguori, V., Moens, F., Peter, J., and Laurendeau, E., "Validation of a nonlinear Vortex Lattice Method for multiple wing sweep angle configurations," *56th 3AF International Conference on Applied Aerodynamics 2022*, Toulouse, France, 2022. URL https://hal.science/hal-03664586.

[29] Wagner, H., "Über die Entstehung des dynamischen Auftriebes von Tragflügeln," *ZAMM - Journal of Applied Mathematics and Mechanics / Zeitschrift für Angewandte Mathematik und Mechanik*, Vol. 5, No. 1, 1925, pp. 17–35. https://doi.org/10.1002/zamm.19250050103, URL http://onlinelibrary.wiley.com/doi/10.1002/zamm.19250050103/abstract.

[30] Jones, R. T., "Operational Treatment of the Nonuniform-Lift Theory in Airplane Dynamics," Tech. rep., NASA, October 1938. URL http://ntrs.nasa.gov/search.jsp?R=19930081472.